

# Sensors, Actuators and Algorithms for Practical Implementations of Turbulence Boundary Layer Control

KENNETH S. BREUER<sup>1</sup>  
Brown University, Providence, RI, USA

## Abstract

The design, fabrication and testing of sensors and actuators for measurement and control of turbulent flows is discussed along with algorithms for real-time feedforward control of turbulent wall bounded shear flows. The advantages and disadvantages of different sensing schemes and designs are reviewed with some recommendations for optimal approaches for sensor design. Examples are drawn from a variety of MEMS sensor programs conducted in our research group over the past few years. A new design for thermal shear stress and temperature sensors is presented. The design of synthetic jet actuators is also reviewed with particular attention on how they might be used in turbulent boundary layer control. Finally, the outline of a real-time control algorithm is described which can be readily implemented in a physical experiment. The results of this experiment are reported, showing excellent performance including uniform reduction of turbulent fluctuation intensities of up to 37% and a decrease in the mean wall shear stress of 7%.

## 1 Introduction

Recent advances in the understanding of near-wall turbulent shear flow structure have resulted in several suggestions for active control including schemes based on qualitative physical arguments (Choi *et al.*, 1994), formal optimal control (Bewley *et al.*, 2001), neural networks (Jacobson & Reynolds, 1998) and reduced-order dynamical representations of the near-wall region (Coller *et al.*, 1994). Several problems, both theoretical and practical face the successful implementation of a real-time turbulence control scheme. From the theoretical side, the complexity of the turbulent boundary layer and its dynamics make the choice of a control algorithm far from intuitive. From the practical side, the spatial and temporal scales at which the control must be executed make the design of sensors, actuators and control hardware very challenging. Many new technologies have arrived in the past few years that will lead to solutions for these problems. In particular, MEMS technology offers an opportunity for the manufacture of small sensors and actuators, while ever-increasing computing power, particularly in DSP technology, allows for real-time implementation of increasingly complex real-time control algorithms.

This paper describes some of the practical aspects of conducting a successful turbulence control experiment, and touches on issues associated with the design and manufacture of sensors and actuators for turbulence measurement and control as well as some control algorithms that have been successfully used to demonstrate real-time control of a low-Reynolds number turbulent flow. Much of the work focusses on results achieved in our own research group, although attempts are made to put these results into a broader perspective. The paper is organized as follows: Section 2 discusses the design and performance of wall-based sensors; section 3 discusses the design and performance of actuators

---

<sup>1</sup>Address: Division of Engineering, Box D, Providence, RI 02912 USA. Email: [kbreuer@brown.edu](mailto:kbreuer@brown.edu). <http://www.microfluidics.engin.brown.edu>

suitable for turbulence control. Section 4 outlines a practical algorithm for feedforward control, and the results of combining all three elements into a closed-loop system are reported in §5.

## 2 Wall-based Sensors

Turbulence measurements for control are, by necessity, restricted to wall-based measurements, so that the flow is not adversely affected by the control system. This restricts us to wall shear stress and wall-pressure measurements. We have, for the most part, focussed on wall-shear stress, since the wall shear signal is very direct and accurate reflection of the turbulence structures in the flow above (Kravchenko *et al.*, 1993), while the pressure is less localized and contains substantial inputs from outer flow large-scale structures.

### 2.1 Sensor Design Considerations

The key tradeoff in the floating element/thermal sensor choice is the advantages and disadvantages of a direct versus an indirect sensor scheme. The floating element would seem to be preferable in this respect, but does have a number of distinct disadvantages, including: It is a planar device - i.e. it is not well suited for installations with high surface curvature. It is also susceptible to streamwise pressure gradients. A pressure gradient over the extent of the device acts on the leading and trailing faces of the floating element to bias the sensor. This effect can be easily shown to be proportional to

$$\text{Error} \propto \frac{dP}{dx} \frac{h}{L} \quad (1)$$

where  $dP/dx$  is the pressure gradient,  $h$ , is the thickness of the floating element and  $L$  is the streamwise extent of the floating element. Thus the aspect ratio of the sense plate (which must be non-trivial in order to ensure structural strength and geometric integrity of the device) becomes critical in the overall sensor accuracy. The device, by necessity contains gaps and small crevices, which can become clogged in a dirty environment. The floating element and/or its supports can be fragile. The mass and stiffness of the floating element significantly affect the frequency response of the device (in macroscopic floating element shear sensors, this issue usually results in large sensors with effectively zero bandwidth).

Thermal sensors also have their pros and cons. While they are inherently indirect measurements, and subject to some calibration procedure, they do not have some of the above-itemized difficulties of floating element sensors (for example, they are sealed and cannot become clogged and they can be conformal to a curved surface). However, the biggest problems with thermal sensors are that:

1. Since they are in close proximity to the surface, a large fraction of their heat is lost to the substrate, resulting in a significant loss in sensitivity
2. Related to this and more serious, unsteady shear effects result in unsteady thermal conduction to the substrate - a process that does not preserve linear phase with increasing frequency. Thus, the sensor has a highly non-uniform phase response with increasing frequency and can yield misleading results in flow fields with high levels of fluctuation (which covers almost every flow field of engineering importance).

There are also some considerations that need to be kept in mind, which are particularly relevant to MEMS devices. Microfabrication is a discipline in which fabrication and manufacturing considerations cannot be separated from design and performance. The integration between the device design and operation, its mechanical and electrical performance is complete. This is in sharp contrast to traditional manufacturing paradigms. The implications of this are that the choice of mechanical and electrical elements, the decision about what kind of transduction scheme to use, and the decision about how to best package the final result are all integrated and all affect the final product. Some concrete implications of this are that: the integration of electronics onto the sensor chip is, at first

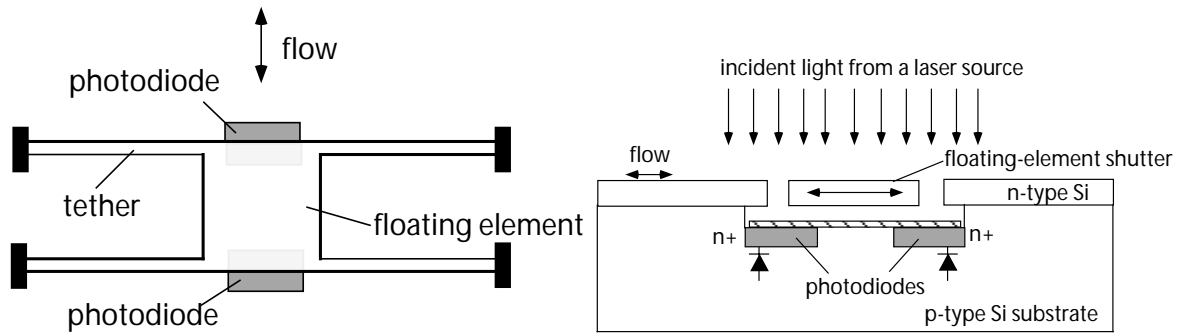


Figure 1: Top and side view schematics of the optical floating-element microfabricated shear stress sensor (Padmanabhan *et al.*, 1996)

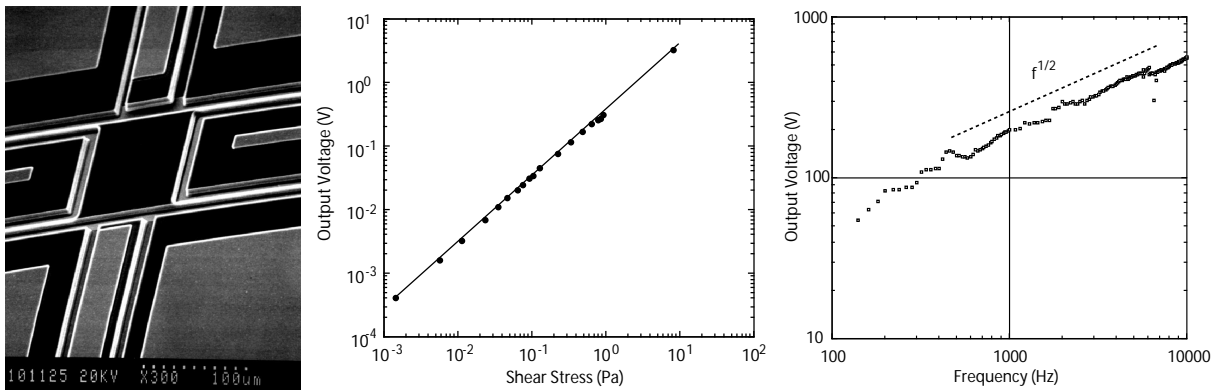


Figure 2: Left frame: SEM Photograph of floating element shear stress sensor. The floating element is 120 microns on a side (Padmanabhan *et al.*, 1996). Center and Right frames: Performance of the optical floating element shear stress sensor. The left frame shows the DC-performance, as calibrated in a laminar flow channel over five decades of shear stress (Padmanabhan *et al.*, 1996). The right frame shows the AC-performance, measured in an acoustic plane wave tube (Sheplak *et al.*, 1998)

blush, appealing and takes advantage of the monolithic nature of micromachining. However, the fabrication requirements of microelectronics and of optimal sensing are often in conflict (for example, electronics cannot tolerate any high temperature processing steps), and thus their integration often results in compromised electronics functionality and compromised sensor design. The choice of materials in MEMS is limited, and their combinations are constrained by processing technology capabilities. Some materials have excellent mechanical properties, but poor thermal or electrical properties, etc. The geometric design, particularly of multi-layer devices is severely constrained by MEMS fabrication technology, which allows only line-of-sight processing. The means to create geometric features thus will result in device design compromises, each of which needs to be balanced one against the other.

## 2.2 Floating Element Sensors

The first micromachined shear sensor successfully demonstrated was that by Schmidt *et al.* (1988), who fabricated a floating element sensor which used the change in capacitance generated by the motion of the sense plate. This device, while revolutionary, had some shortcomings: namely that the primary material used (polyamide) was not a good structural material due to its sensitivity to temperature and humidity, resulting in poor stability.

Secondly, the use of a capacitive transduction scheme has its inherent disadvantages. The change in capacitance is very small and, in order to resolve these small changes, on-chip amplifiers are required to buffer the signal prior to bringing it off chip.

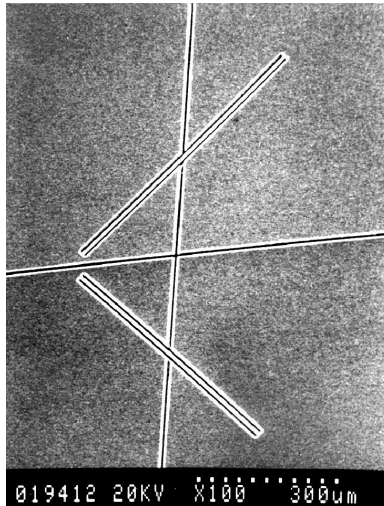


Figure 3: SEM Photograph of thermal flush-mounted "hot wires" with air-gap insulation. The cross through the die defines the four electrical domains needed to drive the two silicon hot wires. Goldberg, Piepsz, Breuer & Schmidt (1995).

As discussed above, the requirement that the sensor and electronics be integrated on the same chip is usually detrimental to the overall sensor design. Lastly, capacitive measurements are, by definition, high-impedance, charge-based, and are very difficult to implement in a low-noise manner. Since the sensor needs to be exposed to the environment, the capacitor plates are vulnerable to stray charges associated with humidity and electromagnetic fields that are commonplace in testing environments. Thus, the sensor is often plagued by noise problems, which are difficult to control.

These problems were addressed, for the most part, by the silicon-based shear sensor of Padmanabhan *et al.* (1996), illustrated in figures 1 and 2. In this design, the basic structure of the sensor was replicated - an H-structure supporting the sense plate. However, in the new design, the entire device is fabricated from single-crystal silicon - an excellent structural material with stable and repeatable mechanical and electrical properties. In addition, in an attempt to avoid the high-impedance capacitive readout of the first generation MEMS devices, Padmanabhan *et al.* (1996) utilized a pair of photo-diodes, differentially obscured and revealed by the motion of the floating under the action of shear. This device achieved all of its goals - stable operation and high sensitivity, as illustrated in figure 2 which shows the static calibration and demonstrates a linear relationship between output voltage and shear over five decades of shear, with sensitivity as low as 0.002 Pascal. The unsteady performance of the floating element optical sensor was demonstrated by Sheplak *et al.* (1998), who calibrated the sensor in an acoustic plane wave tube (figure 2) and showed a uniform response ( $\pm 3\text{dB}$ ) up to the limit of their calibration facility (10 kHz).

However, the optical shear sensor was not without its difficulties. The original sensor design was overly sensitive to variations in the incident illumination field, and to variations in temperature which affect the photo-diode performance. These problems were corrected in a subsequent design (Sheplak *et al.*, 1998), but the sensor was nevertheless not widely tested or used in experimental testing (a victim of research funding shortfalls).

### 2.3 Thermal Shear Sensors

As discussed above, hot film sensors are particularly sensitive to parasitic losses to the underlying substrate, which severely limit their sensitivity and frequency cutoff and can induce non-uniform phase response. An example of a microfabricated sensor which was compromised by this problem is shown in figure 3 which shows an SEM of a pair of flush-mounted silicon "hot wires" fabricated by Goldberg *et al.* (1995). Here, the sensing element is a thin single crystal silicon hot wire through

which a current is passed. The wire heats up and, much as a conventional hot film operates, responds indirectly to shear stress due to convective cooling by the flow over the sense element.

In this design, the thermal isolation is provided by a thin air gap, 5 microns to each side and below the hot wire. In retrospect, it is clear that this was not an adequate insulation layer, and the testing confirmed that, when a current was passed through the wire, the entire chip heated up to a temperature close to that of the hot wire itself. This resulted in a very large thermal mass acting as the sense element, and consequently very poor temporal performance.

This device, despite its shortcomings, did work and did illustrate an important breakthrough in microfabrication - the ability to fabricate backside electrical contacts. These contacts were achieved using a process that enabled the electrical connections to be made from the rear of the chip, thus leaving the flow field undisturbed. This, as mentioned above, is a key difficulty with MEMS sensors, and is a particularly important hurdle to cross in aerodynamic testing where preservation of the surface finish can be very important.

MEMS sensors which substantially reduced the problems of thermal leakage were presented first by Lui *et al.* (1995) who developed a series of shear sensors in which the sensor was mounted on a membrane over an evacuated cavity. In this case, the parasitic losses were confined to conduction losses through the thin membrane and through the electrical leads to the sensing element, which in the case of the Lui *et al.* (1995) sensor, was fabricated from polysilicon.

If one assumes that the sensor will be operated in constant temperature mode (as is usually the case), a simple analysis is instructive in illuminating the relative importance of design choices.

We first assume that the power,  $P$ , dissipated by the sensor is generated by Ohmic heating of the sensing element:

$$P = I^2 R = \frac{V^2}{R} \quad (2)$$

where  $V$ ,  $I$  and  $R$  are the voltage, current and sensor resistance respectively. We also assume that the sensor resistance has the typical linear dependence on temperature:

$$R = R_o(1 + \alpha\Delta T) \quad (3)$$

where  $R_o$  is the cold resistance,  $\Delta T$  is the change in temperature (above ambient) and  $\alpha$ , the temperature coefficient of resistivity, or TCR. The power is dissipated by convection to the flow above the sensor (represented by a generalized convection coefficient,  $h$ ) and by conduction to the substrate below (represented by a generalized conduction coefficient,  $k$ ):

$$P = (k + h(\tau_w))\Delta T \quad (4)$$

The conduction is assumed to independent of velocity. Equating the power generated with the power dissipated, and solving for voltage we find that

$$V^2 = (k + h(\tau_w))\Delta T \cdot R \quad (5)$$

We are interested in the sensitivity of the device, which is found by differentiating with respect to shear and dividing by voltage to get a normalized sensitivity:

$$\frac{1}{V} \frac{\partial V}{\partial \tau_w} = \frac{1}{2} \frac{\partial h}{\partial \tau_w} \frac{\Delta T R}{V^2} = \frac{1}{2} \frac{\partial h}{\partial \tau_w} \frac{\Delta T}{P} = \frac{1}{2} \frac{\partial h}{\partial \tau_w} \frac{(R - R_o)\alpha}{P R_o} = \quad (6)$$

Thus, in order to maximize sensitivity one wants to maximize the operating temperature while minimizing the dissipated power. This is achieved using small thermal masses (less power) and materials with high TCR (high temperature differences for a given resistive overheat setting).

Parasitic thermal losses typically arise due to two sources: conduction through the electrical leads to the substrate and conduction through the supporting structure to the substrate. Conduction through the electrical leads is clearly unavoidable and there is little one can do to affect it. To minimize power dissipation in the leads, their electrical resistance needs to be low which is achieved

by low resistivity material coupled to a high cross-sectional area. However, low resistivity is usually correlated with high thermal diffusivity, and thus low electrical resistance almost guarantees high thermal conductivity. One should note that the same problem exists with conventional hot wires. In both cases the problem is minimized by making the sensor element have high aspect ratio so that the cross sectional area responsible for heat transfer to the flow is as high as possible, compared to the cross sectional area responsible for parasitic conduction to the electrical leads.

Parasitic conduction directly to the substrate is minimized in the thermal shear sensor by mounting the sensor on a vacuum-backed cavity, as was demonstrated by Lui *et al.* (1995). In this case, the leakage path is restricted to conduction along the surface of the membrane. Again, a simple analysis is instructive.

We consider a shear stress with a characteristic radius  $r = R_i$ , mounted on a membrane of radius  $r = R_o$ . If we assume that the temperature is uniform through the thickness of the circular membrane film at any given radial location (a reasonable assumption for a thin supporting membrane), we can model the temperature distribution as being a function only of radial distance. The sensor element maintains a high temperature  $T_i$  at the sensor element near the center ( $r = R_i$ ), while it drops off to ambient temperature,  $T_o$ , at the edge ( $r = R_o$ ). Simple heat conduction theory yields the solution for the one-dimensional temperature distribution in the membrane:

$$T(r) = T_i + (T_o - T_i) \frac{\ln(r/R_i)}{\ln(R_o/R_i)} \quad (7)$$

and gives the total heat flux,  $q$ , leaving the membrane at  $R_o$  as

$$q \propto \frac{kt(T_o - T_i)}{\ln(R_o/R_i)} \quad (8)$$

where  $k$  is the thermal conductivity and  $t$  is the membrane thickness. To minimize this for a given temperature difference and a fixed sensor size,  $R_i$ , we clearly want to make the ratio

$$\frac{t}{\ln(R_o/R_i)} \quad (9)$$

as small as possible. This however is limited by the fact that the membrane also has a structural function and needs to support a pressure difference - atmospheric on one side and vacuum on the other. This pressure difference must be balanced by the biaxial stress,  $s$ , in the membrane:

$$s^2(s - s_o) = \frac{Mp^2R_o^2}{24t^2} \quad (10)$$

where  $M$  and  $s_o$  are the biaxial elastic modulus and residual membrane stress (material or processing properties and assumed to be constant);  $p$  is the supporting pressure (1 atmosphere). Assuming that the total biaxial stress,  $s$ , is limited by some (fixed) upper value beyond which the membrane will fracture, we see that

$$\frac{R_o}{t} = \text{constant}. \quad (11)$$

These two constraints are optimized making  $t$  as small as possible and then choosing  $R_o$  as large as it can be to mechanically support the membrane. In addition, the membrane should be manufactured with as little residual stress ( $s_o$ ) as possible.

## 2.4 New Thermal Sensor Design

With these considerations in mind, a new sensor was designed and fabricated by Breuer *et al.* (1999) and is illustrated in figure 4. The sensor design is based on two key goals:

- Minimize the thermal mass of the sensor to maintain a high frequency response. This requires that the sensor element be small and (more importantly) that the sensor be thermally isolated from the substrate as discussed above.

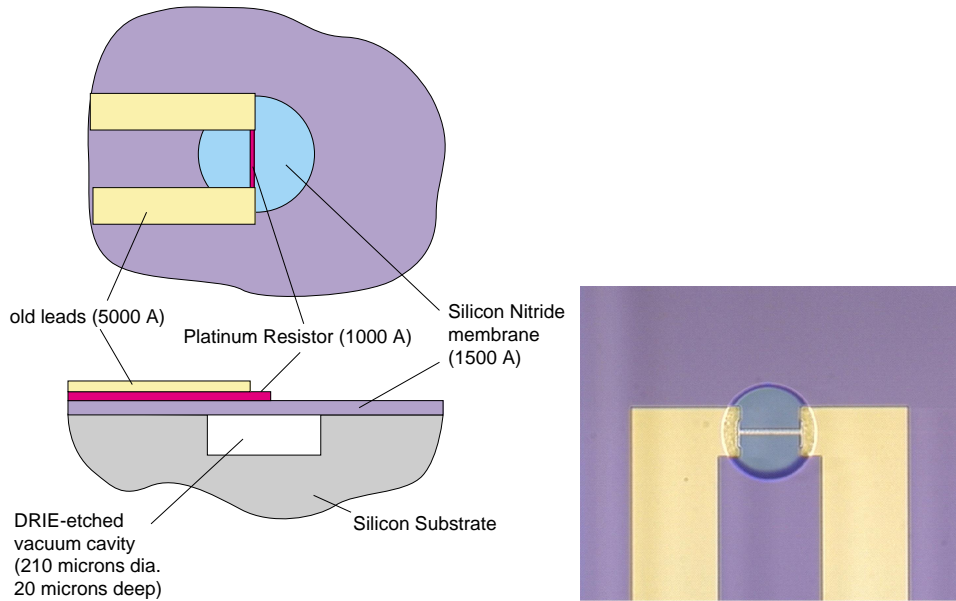


Figure 4: Schematic of Thermal Shear sensor/temperature sensor design (left) and optical micrograph of the completed sensor (right). The sensor element is mounted on a thin membrane, which covers a vacuum cavity.

- Keep sensor resistance low (to keep noise down, sensitivity high and to allow for standard anemometer circuits to be used).

The fabrication of the sensor was achieved by using a very thin silicon nitride membrane (1500-Å) which covers a deep (20 micron) evacuated cavity. The vacuum cavity eliminates direct conduction to the substrate while the thin membrane limits the thermal conduction path through the membrane. The electrical connections are achieved using the sensor metal, which is platinum (and has a very high temperature coefficient of resistivity) and a second layer of gold, which serves to minimize the lead resistance. The cavity thickness and diameter were sized to optimize the trade-off between membrane conduction losses and membrane deflection and fracture strength as discussed above. This optimization resulted in a membrane 210 microns in diameter and 1500 Angstrom thick.

To minimize the direct thermal mass of the platinum, the resistors were fabricated as small as possible, limited by lithography. Line widths of 3, 5 and 10 microns were attempted although it was found that 3 microns was not reliable. Since the leads to the resistor serve as a parasitic loss, their resistance was minimized by increasing their cross-sectional area and by depositing 5000-Å of gold on top of the platinum used as the resistor. In the final device, the resistance of each lead was 2% of the sensing resistor.

## 2.5 Device Performance

The completed devices is shown in figure 4 (right frame). The sensing element is the thin line crossing horizontally across the vacuum-backed membrane, which is visible as the light-colored circle. The deflection of the cavity under the atmospheric pressure loading is clearly visible. Figure 5 (left frame) illustrates the response of the current-voltage characteristics for a 100-micron resistor long 5-micron wide shear sensor. Both ascending and descending applied voltages are plotted demonstrating the lack of hysteresis. The positive curvature illustrates the Ohmic heating at high current which results in an increase in the sensor temperature (the effect that is used to operate the wire as a fluid sensor). In this case, the (DC) resistance changes by a factor of two, rising from approximately 50 Ohms to about 90 Ohms at 10 mA (approximately 9mW power dissipation). The sensor was operated using a constant temperature anemometer circuit at a resistive overheat of 1.4. Initial testing revealed that the sensor tended to drift due to the cold resistance of the wire decreasing as a function of time. However, the

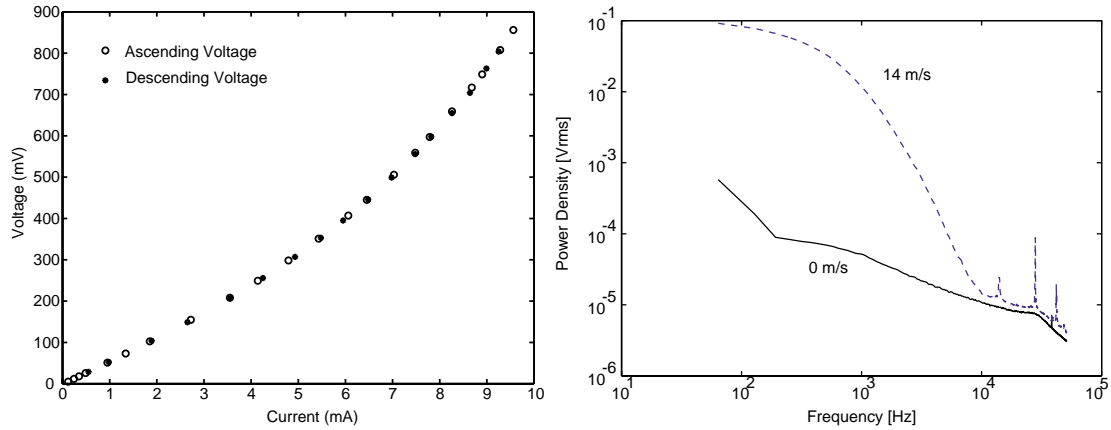


Figure 5: Performance of the thermal sensor. The left frame shows the Voltage-Current behavior of hotwire sensors ( $5 \mu\text{m} \times 100\mu\text{m}$  long) sensor on a vacuum cavity. The positive curvature indicates self-heating due to Ohmic losses. The right frame shows the Power Spectrum response of the sensor as measured in a fully turbulent boundary layer and compared with the zero-flow spectrum

drift disappeared after some hours of operation as the wire resistance stabilized. The source of this drift was not immediately evident but might be due to either some annealing of the metal layers as they were operated, or the burning off of some residual materials remaining from the processing and packaging operations.

The sensors showed excellent performance with good frequency response (square-wave response test was limited by the anemometer circuitry which rolled off at 40 kHz). Figure 5 shows a typical power spectrum taken with no flow and then under a turbulent boundary layer at approximate Reynolds number (based on distance from the leading edge of the flat plate) of 1 million. An excellent signal-to-noise ratio is observed, and this could probably be improved further by using more sensitive anemometer electronics or perhaps a greater overheat ratio.

## 2.6 Flush Wire Shear Sensors

While MEMS sensors are appealing due to their compact nature and high possible performance, it is difficult, in a research environment, to manufacture them in sufficient quantities for a control experiment, and to integrate them easily into a real experiment. For this reason, traditional flush-mounted hot wires have also been used as shear sensors for control inputs (particularly in the experiments of Rathnasingham & Breuer (1997b, 2002)). In these cases, the sensors are simply hot wires, mounted flush to the surface and sensitive to local shear. Rathnasingham & Breuer (1997b) reported that the shear sensors were more effective when they were oriented so that the hot wire was parallel to the mean flow, rather than perpendicular, as is the usual orientation. In this parallel mode, the wires are primarily sensitive to the absolute value of the spanwise shear fluctuations, but also retain some sensitivity to streamwise shear fluctuations. The improvement in control performance due to this unconventional use of the shear sensors is still an issue that needs to be explored, but it is consistent with numerical observations Lee *et al.* (1997) that the spanwise shear is an effective control input for turbulent shear flows. However, a second practical aspect of the sensor configuration is also worth noting: the alignment of the wire gives the sensor extremely good spatial resolution in the spanwise direction (limited by the thickness of the sensing wire which for the experiments of Rathnasingham & Breuer (1997b) was  $2.5 \mu\text{m}$  - less than  $l^*/20$ ).

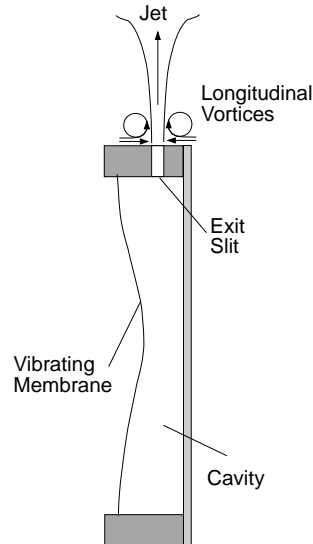


Figure 6: Schematic diagram of a synthetic jet actuator optimized for boundary layer control, with the resultant jet flow out of the exit slit.

### 3 Actuators

The requirements for control actuators are similar to that of sensors - flush mounted and unobtrusive. However, the progress in actuators has been much less successful than that of sensors. Several actuators for flow control have been proposed, ranging from direct injection of heat (Liepmann *et al.*, 1982) to controllable bumps (Grosjean *et al.*, 1998). However, the most successful to date has been the so-called “synthetic jet”, first demonstrated by Ingard (1953), but popularized in recent years by Glezer and his co-workers (Glezer & Amitay, 2002, for example). These devices are described in the current paper, since they were used in the control demonstration of Rathnasingham & Breuer (1997b, 2002) and continue to hold promise for future applications.

#### 3.1 Synthetic Jet Actuators

##### 3.1.1 Operating Principles

A schematic of a synthetic jet, as used by Rathnasingham & Breuer (1997b, 2002) is illustrated in figure 6. The device consists of a cavity open to the flow by a small slit through which fluid is free to move. The cavity is driven by a moving surface, either a piston, loudspeaker or vibrating membrane (as in the case illustrated here). As the membrane compresses the cavity, fluid is pushed out of the cavity and as the membrane moves back, fluid is sucked back into the cavity. For small displacements, the flow is reversible and no net motion is observed. However, at a certain amplitude, the outflow separates at the exit corner and a vortex ring is formed which moves away from the device. The backstroke replenishes the cavity, but due to the asymmetry of the flow, the inward flow draws uniformly from the flow outside the cavity. Thus, over a cycle, or many cycles, a jet flow is generated in which fluid is drawn in from the sides and pushed upwards by the actuator’s motion.

Several modifications of the device can be used to enhance and modify the flow. For example, two devices side-by-side can be phased to yield a vectored jet (Glezer & Amitay, 2002). The devices have also been microfabricated, as reported by Coe *et al.* (1994), and the structural and fluid mechanics of the synthetic jet have been extensively studied by several researchers, including Rathnasingham & Breuer (1997a) and Lee & Goldstein (2001) who have conducted theoretical and numerical studies respectively.

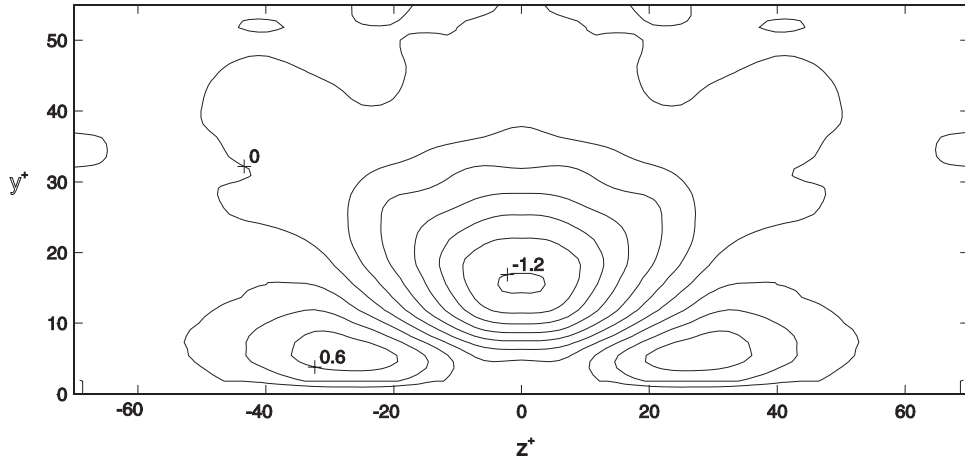


Figure 7: Contour plots of the change in the mean streamwise velocity at  $60l^*$  downstream of the end of the actuator opening slit. The vortices have maintained their relative positions (separated by  $40l^*$  or 4 slit widths and centered about the slit) as they convected downstream. The contour levels are in increments of  $0.2 u^*$ . (Lorkowski *et al.*, 1997).

### 3.2 Actuator Design and Characterization

In the present case, the actuator shown in figure 6 is particularly adapted for turbulent boundary layers, since it has a low-area face exposed to the flow which allows for close packing in the spanwise direction. The exit slit, measuring  $10l^*$  by  $150l^*$ , is aligned in the streamwise direction and the resultant outflow consists of a plane jet directly over the slit together with a pair of counter-rotating streamwise vortices on either side. This streamwise vortex pattern is similar to that used by Jacobson & Reynolds (1998) in their study of control of vortices in laminar boundary layers. The dynamics of the actuator is expressed in terms of a transfer function between an input voltage and the jet velocity. The transfer function exhibits a resonant peak at 2.3 kHz. To illustrate the mean effect of the jet on the near-wall region Lorkowski *et al.* (1997) measured the streamwise velocity just downstream of an actuator slit while operating at a constant amplitude (steady forcing). Figure 7 illustrates the flow pattern as a contour map (in the  $y - z$  plane) of the increase in the mean streamwise velocity. The vortical structures are centered about the slit and are seen to be approximately  $10l^*$  in diameter and are separated by  $40l^*$ . Further details regarding the characteristics and evolution of these vortices are discussed by them. They also measured mean and root-mean-squared streamwise velocity profiles downstream of the actuator.

Figure 8a is a plot of the mean profile taken directly downstream of the actuator. It illustrates the region of lower-speed fluid that results from the effect of the actuator output jet. The root-mean-squared profile (figure 8b) indicates that the location of its maximum is located further from the wall, suggesting that the point of maximum turbulent production may also be shifted further out into the boundary layer.

## 4 Control Algorithms

### 4.1 Theory of Feedforward Control Strategy

While there have been many elegant and effective approaches to turbulent boundary layer control using numerical experiments (Choi *et al.*, 1994; Bewley *et al.*, 2001; Bewley, 2001), little attention has been paid to practical implementations of control where the real-life issues of limited numbers of sensors and actuators, as well as limited real-time processing power need to be addressed. The following section reviews one particular approach to this problem, as reported by Rathnasingham & Breuer (1997b, 2002). It is, to our knowledge the only example of a real-time closed-loop experimental

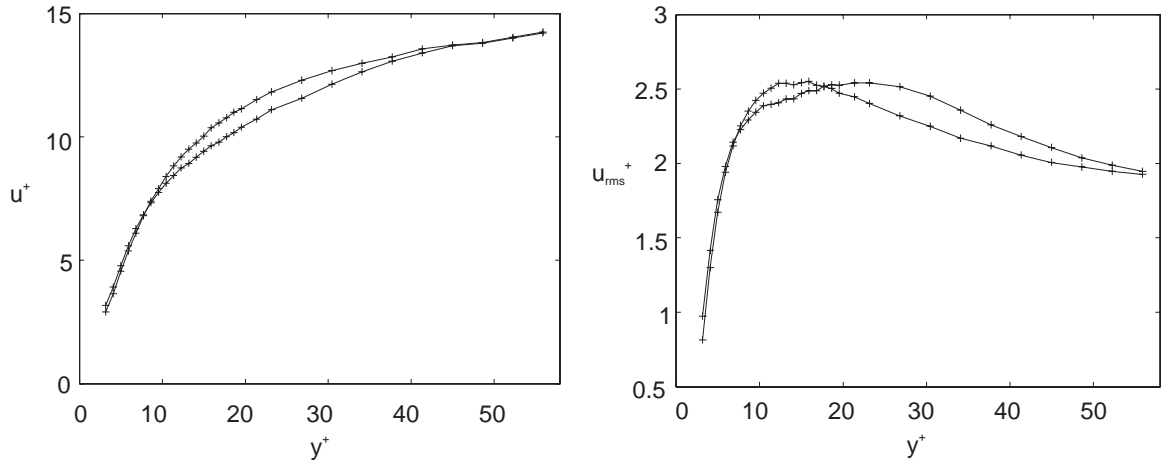


Figure 8: Mean and root-mean-squared profiles,  $60l^*$  downstream of the actuator. The injection of low-speed fluid is seen in the mean profile, while the root-mean-squared profile shows a maximum value further away from the wall in the forced case. (Solid line: unforced, dashed line:forced) (Lorkowski *et al.*, 1997).

demonstration of turbulence control.

The control approach is based on two key assumptions, namely: (i) that the majority of the turbulence-producing events in the near-wall region of the flow are associated with the large-scale “coherent structures” and (ii) that these coherent structures may be modelled (for short times) by dynamical equations which are linear with respect to the mean flow. The first assertion is supported by a large body of research on coherent structures over the past twenty years, and is well-illustrated in the analysis by Johansson *et al.* (1991) of numerically-generated turbulence in which they report that the coherent structures, while only occupying 25% of the volume in the near-wall region, are responsible for 50% of the total turbulence production. The assumption of linearity is based on the observation that the strong mean shear of the near-wall turbulent flow will dominate the short-time evolution of small perturbations. This is consistent with the framework provided by the Rapid Distortion Theory of turbulence (Hunt & Carruthers, 1990) and other models for near-wall turbulence (Landahl, 1990). In addition, experiments Johansson *et al.* (1987) have found that conditionally-sampled  $u$ ,  $v$  and  $p$  signals scaled linearly with threshold amplitude, again suggesting an amplitude-invariant behavior for these coherent structures. For the purposes of control, this linearity assumption need only hold for the short time it takes a structure to advect from an upstream sensor to an actuator and does not imply that turbulence production as a whole is governed by a linear mechanism. It is interesting, and re-assuring to note that since the completion of this experiment, other evidence for the success of linear schemes applied to the control of turbulent flows has also been presented, notably by Bewley (2001) and by Lee *et al.* (2001).

Given these working assumptions, the control strategy pursued in these experiments is shown schematically in figure 9. A multiple-input, multiple output (MIMO) linear filter (Bendat & Piersol, 1971) is constructed as an estimate of the transfer function between signals from a spanwise array of upstream wall-based sensors (in this case from three sensors:  $s_1(t)$ ,  $s_2(t)$  and  $s_3(t)$ ) and the signals from sensors located at downstream “control points” (again, in this case, three sensors:  $c_1$ ,  $c_2$  and  $c_3$ ). The estimated transfer function is represented in figure 9 as  $\hat{H}$ , while the physical (true) relationship between the upstream and downstream sensors is indicated by  $H$ . In general  $H$  will not be equal to  $\hat{H}$ , the difference resulting from both nonlinear relationship between the two arrays of sensor signals and the fact that the signals at the downstream sensor array will also be affected by other inputs not sensed by the upstream sensor array (for example, outer-flow effects, etc).

In a similar manner, we construct a linear transfer function between an array of  $P$  actuators (in this case  $P = 3$ ) and each of the downstream control points. This is represented by  $\hat{G}$  and, as before,

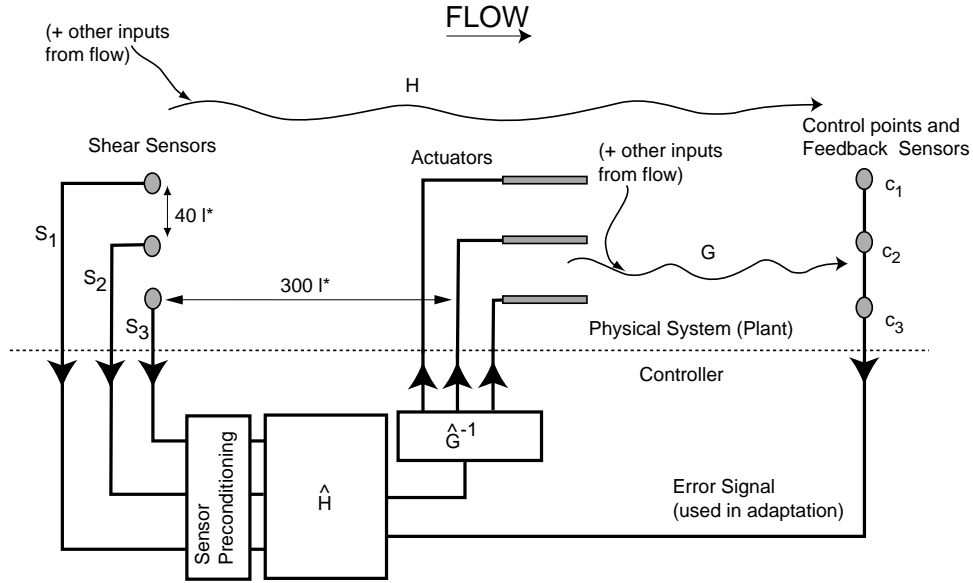


Figure 9: Schematic diagram showing the plant - the turbulent boundary layer - together with detection sensors ( $s_1, s_2, s_3$ ), actuators ( $a_1, a_2, a_3$ ) and downstream control points ( $c_1, c_2$  and  $c_3$ ). The block diagram below the dotted line represents the controller including the adaptive feedback path.  $H$  and  $G$  are actual transfer functions, while  $\hat{H}$  and  $\hat{G}$  are their linear estimates, derived from cross-correlation measurements.

the “true” relationship between the actuators and  $c_i$  is nonlinear and includes additional inputs, not captured by this representation.

With these two transfer functions (or, more correctly, systems of transfer functions), we invert the actuator transfer function and construct a feed-forward control system,  $\hat{H}\hat{G}^{-1}$  such that if  $\hat{H}$  and  $\hat{G}$  were completely accurate descriptions of the full system, the fluctuating signal at each control point,  $c_i$  would be zero. In reality, small variations, slow changes and, more-importantly, nonlinearities and non-observed inputs will result in an error at the control points such that the difference between the predicted signal at the control points and the observed signal will not be identically zero. However, this error can be further minimized, and maintained at a low level by employing an adaptation scheme. Typical adaptation schemes include perturbing the filter coefficients, either randomly or by some proscribed adaptive optimization scheme. In this manner, the overall control performance can be optimized or adapted to suit changing freestream conditions.

This control approach is quite general and may be applied to an arbitrary number of upstream sensors, actuators and downstream sensors (control points). It has several appealing features, namely:

1. The control points define what the control objective is. for example, to reduce the level of fluctuations at the control point sensors, the control signal that the actuators will attempt to minimize is simple the rms fluctuations. To reduce the mean turbulent drag, the control signal is simply the mean shear stress, to reduce the turbulent-induced wall pressure fluctuations, the rms-wall pressure fluctuations are used as control point inputs. These control objectives are different and will not necessarily result in the same control scheme. However, they all can be treated using this approach.
2. In its most general sense, the control filters depend on inputs that can derive from both space and time. For example, one possible series of filters could be constructed from a large spatial template of wall sensors, all sampled at a single time. A second extreme might be a filter constructed from a single sensor, sampled over time and used to construct the estimate at the control point. The optimal filter is one that contains both spatial and temporal information.
3. The filters are pre-computed, and only require low-bandwidth adaptation to maximize their per-

formance. This architecture enables practical implementation (unlike some of the more complex neural network or optimal control schemes which, though theoretically attractive, cannot be tested physically).

4. The template of transfer functions is finite and independent of what goes on in the rest of the flow. This means that control is local and can be implemented using an overlapping network of local controllers (again, an attractive feature for realistic implementation) with only moderate “supervisory” attention to optimize and update filter coefficients to account for slow changes in the mean flow. This local nature of the control allows for complete scalability to larger areas of control authority. The local processing power need not become more powerful, only more dense.

## 4.2 Sensor Pre-conditioning: Detection of Coherent Structures

Central to the success of this scheme is the ability to accurately predict the flow state at the downstream sensors,  $c_i$ , using the upstream wall sensors,  $s_i$ . For the turbulent boundary layer, the dominant contribution over such large distances is by the large-scale coherent structures. However the “footprint” of the coherent structures is contaminated by random variations and small scale fluctuations. Thus the chief problem of prediction becomes one of (i) identification of the large scale structures and (ii) prediction of their evolution. If we assume that we can define large scale structures statistically, i.e. any signal that retains finite correlation over some spanwise distance, then the identification can be efficiently achieved using a *conditioned spectral analysis* (Bendat & Piersol, 1971) which isolates the correlated portion of (any) two signals. This is best expressed in the frequency domain:

$$\begin{aligned} S_{12}^c(\omega) &= \frac{\Phi_{12}(\omega)}{\Phi_{22}(\omega)} S_1(\omega) \\ &= L_{12}(\omega) S_1(\omega). \end{aligned} \quad (12)$$

where  $S_{12}^c$  is the correlated part of the two signals  $S_1$  and  $S_2$  ( $s_1(t)$  and  $s_2(t)$  expressed in the frequency domain),  $\Phi_{12}$  and  $\Phi_{22}$  are the cross-spectra and auto-spectra respectively. Note that for a spatially homogeneous field (such as the spanwise direction in a turbulent boundary layer),  $S_{12}^c$  is identical to  $S_{21}^c$ .

The rest of the signal makes up the uncorrelated portion,

$$S_{12}^u(\omega) = S_1(\omega) - L_{12}(\omega) S_1(\omega). \quad (13)$$

The conditioning filter,  $L_{12}$ , is nothing more than a linear filter which pre-conditions the input signals weighting them to favor a frequency band statistically determined to be most highly correlated. In this sense, it is a rather crude pre-conditioning and many more complex pre-conditioning schemes can be envisaged, particularly if a dynamic model of the near-wall region of the boundary layer were available, in which case a Kalman filter could be constructed as demonstrated in a numerical flow, for example by Podvin & Lumley (1998). This would give a real-time identification of large-scale structures and, presumably, a superior performance over the simple case presented here.

## 4.3 Forward Prediction and the Wiener Filter

With the pre-conditioned input signals, we now need to assemble the filter that will predict the evolution of the large-scale structures ( $\hat{H}$  in fig 9). We consider a system with  $i = 1 \dots N$  input signals a single control point  $c$ . The predicted signal at the control point at any given time,  $t_o$  is described by a weighted sum:

$$c(\hat{t}_o) = h_1 s_1 + h_2 s_2 + h_i s_i + \dots + h_N s_N \quad (14)$$

where  $s_i$  are discrete measurements from the  $N$  sensors, and  $h_i$  are the corresponding linear weights (assumed constant). Note that the  $s_i$  are discrete measurements from *any* combination of spatially or

temporally distinct sensors. For example  $s_1$  could be a measurement from an upstream shear sensor, sampled at  $t = t_o$ ;  $s_2$  might be a measurement from the same sensor, but sampled at a previous time,  $t = t_o - \Delta t$ ;  $s_3$  might be a measurement from a different sensor, sampled at  $t = t - 2\Delta t$ , and so on. (The implications of this will be discussed in the next section).

The values of  $h_i$  are found by minimizing the mean-square error between the real measurement at the control point  $c(t)$ , and the predicted measurement at the control point,  $c(\hat{t})$ . This least-squares minimization procedure is simply one definition of the Wiener filter (Bendat & Piersol, 1971), and after some rudimentary calculations, we find that the linear weights,  $h_i$  are found as the solution to the matrix equation:

$$\begin{bmatrix} \Phi_{11} & \Phi_{12} & \dots & \Phi_{1N} \\ \Phi_{21} & \ddots & & \\ \vdots & & \ddots & \\ \Phi_{N1} & & & \Phi_{NN} \end{bmatrix} \begin{bmatrix} h_1 \\ h_2 \\ \vdots \\ h_N \end{bmatrix} = \begin{bmatrix} \Phi_{1c} \\ \Phi_{2c} \\ \vdots \\ \Phi_{Nc} \end{bmatrix} \quad (15)$$

where  $\Phi_{ij}$  is the mean cross-correlation between different input signals:

$$\Phi_{ij} = \langle s_i s_j \rangle \quad (16)$$

and  $\Phi_{ic}$  is the cross-correlation between each input signal and the control point.

$$\Phi_{ic} = \langle s_i c \rangle \quad (17)$$

These cross-correlations can be computed and the matrix inverted to yield the linear weights. The process can be repeated with different right-hand-sides to find weights appropriate for different control points.

#### 4.4 Filter Design Flexibility

As mentioned above, the input measurements can be taken from any point in space or time. This flexibility has many interesting implications, a few of which are discussed here. If all the inputs are taken from spatially distinct sensors at a single time,  $t = t_o$ , and they used to predict the flow at the control point at the same time,  $t_o$ , then the Wiener filter will contain no flow history, but will rely solely on the spatial pattern of the flow to predict its state at some other point. This was demonstrated Almonlirdvirman & Breuer (2000) using the flow from a low-Reynolds number turbulent database. It is also identical (mathematically) to the Stochastic Estimation procedure of Adrian (1994). At the other extreme, if we use a single sensor, but sample it at many times and use that time history to predict the flow at some later time, then we are relying solely on the temporal evolution of the flow at a single point to predict the state of the flow at some other point. The linear filter (14) then reduces to

$$c(t_o) = h_o(t_o) + h_1(t_o - \Delta t) + \dots + h_i(t_o - i\Delta t) + \dots h_N(t_o - N\Delta t) \quad (18)$$

from which it is easy to see that the elements of the matrix in the Wiener filter equation (15) reduce to the standard auto and cross-correlation functions,  $R_{ss}(\tau)$  and  $R_{sc}(\tau)$ .

Clearly both of these extremes are limited in their ability to accurately predict the flow at some remote point in space and some future time, and the optimal filter must contain some spatial information (derived from distinct input sensors) as well as some temporal history (derived from a time sequence sampled at each sensor). These can be played off each other, and more temporal information can compensate to some extent for limited spatial information (and vice versa). This is the common dilemma faced between numerical studies of control in which spatial information is usually ‘‘cheaper’’ than temporal information, and the current approach, in which temporal information is much easier to obtain than spatial information.

Another interesting implication of this approach stems from the fact that the forward prediction equation (14) can use sensor inputs that come from times in the future ( $t > t_o$ ). It is, of course not

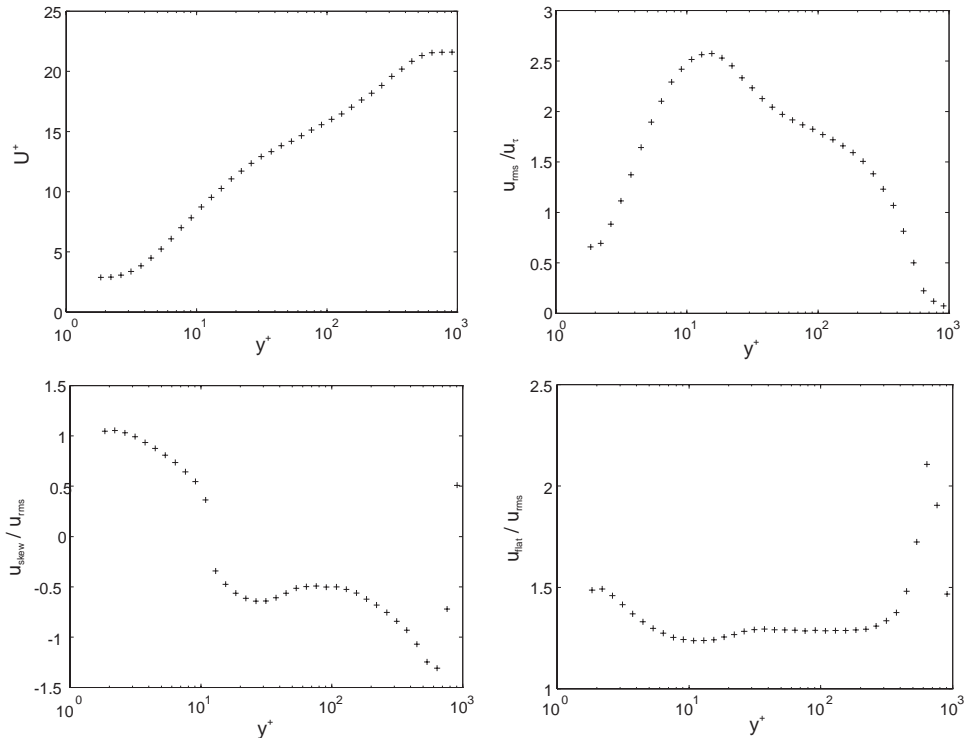


Figure 10: Wall-normal profiles of the first four statistical moments of the streamwise velocity in the baseline (uncontrolled) turbulent boundary layer ( $Re_\theta = 1960$ ).

physically possible to implement this kind of filter, which represents an Infinite Impulse Response linear filter (IIR), in contrast to the finite impulse response (FIR) filter which derives from physically realizable measurements taken at times equal to or less than the current time. However, IIR filters are often re-cast as recursive filters that can be physically implemented. This is commonly done in control systems design, but can be difficult and is beyond the scope of the current discussion.

#### 4.5 Filter Inversion

Using the methods described above, an array of  $M$  forward-prediction filters,  $\hat{H}$  can be constructed connecting arbitrary sensor inputs to each of the  $M$  control points. In the most general form this leads to  $M$  filters, each with  $N$  weights. Similarly, the relationship between each of the  $P$  actuators and each of  $M$  control points can also be identified by simply measuring the transfer function (i.e. cross-correlation) between a signal injected into the actuator and the correlated response at each of the control points. This results in  $P \times M$  filters representing  $\hat{G}$  in figure 9. In order to make this system operational, the filter system is then inverted to form a single system of filters which takes the sensor measurements and results in an input to the actuators such that the optimal (Weiner) filter design is satisfied. The complete details of this are reported by Rathnasingham (1997) and Rathnasingham & Breuer (2002).

### 5 Experimental Results

Having laid the groundwork for the design of the hardware and the control scheme, we present a small-scale demonstration of its performance. In the current experiment a limited patch of turbulent boundary layer is controlled using three input sensors, three actuators and three control points. The description here is, by necessity of space, rather terse. The full details are reported by Rathnasingham & Breuer (1997b, 2002).

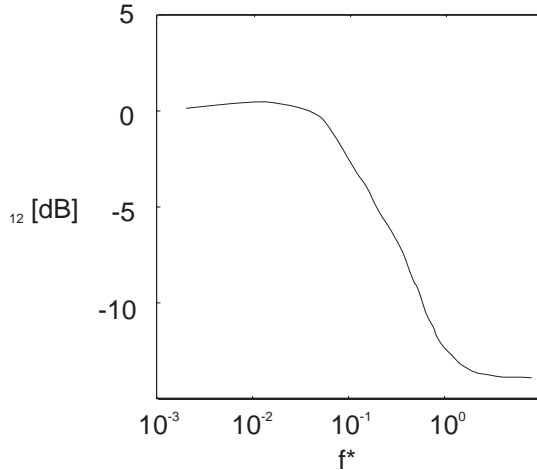


Figure 11: The filter  $L_{12}$  illustrating the emphasis of the low frequency scales. The filter was used to condition the signals from the detection sensors so as to extract the large scale motion in the flow.

## 5.1 Experimental Setup

All experiments were carried out in a Low Turbulence Wind Tunnel previously described by Breuer *et al.* (1996). An aluminum flat plate was mounted vertically in the wind tunnel test section which measures  $0.3 \times 0.6$  m in cross section, and 3 meters in length. A roughness strip 10 cm downstream of the leading edge tripped the boundary layer which was then allowed to grow undisturbed. Careful measurements ensured the existence of a canonical zero-pressure gradient turbulent boundary layer. The Reynolds numbers based on downstream distance from the leading edge and momentum thickness are  $8.1 \times 10^5$  and 1960, respectively. The corresponding viscous length and time scales are  $55 \mu\text{m}$  and  $270 \mu\text{s}$ , respectively. To ensure the statistical convergence of the measured data, record lengths are based on a 95% confidence level with a 0.2% uncertainty in the root-mean-squared value. This resulted in data records that contained  $2 \times 10^6$  independent sample points each. The active control system was managed with a 60 MHz DSP-based real-time signal processing board embedded into a desktop PC. The board was capable of running the control system (three inputs and three outputs in the cases presented here) at a maximum of 35 kHz ( $9.5f^*$ ) - much faster than was actually required. Further details of the implementation of the control loop are discussed by Rathnasingham (1997).

The baseline turbulent boundary layer velocity profiles are shown in figure 10. These profiles, and all subsequent boundary layer measurements were obtained using a single-wire hot wire probe,  $2.5 \mu\text{m}$  in diameter, operated at a resistive overheat ratio of 1.6. The probe was mounted on a traversable sting controlled by the lab computer. The profiles compare well with past low-Re data (Purtell *et al.*, 1981). The mean velocity profile is seen to exhibit a linear near-wall region for  $y^+ < 7$ , a log-law region for  $30 < y^+ < 100$  and a outer wake region for  $y > 200$ . The logarithmic region is well matched to the Clauser profile with a gradient of 2.5 and an intercept of 5.0 (Schlichting, 1968). The mean wall shear stress, obtained using the Clauser profiles, was equal to  $0.116 \text{ N/m}^2$ , corresponding to a friction velocity,  $u_\tau = 0.31 \text{ m/s}$ . The peak value in the root-mean-squared profile ( $u_{rms} = 2.6u_\tau$ ) occurs at  $y^+ = 12$  and coincides with the zero-crossing of the skewness and the point of minimum flatness.

The controlled region of the flow is as shown in figure 9. Three wall-based sensors were used as control inputs. These were coupled to three synthetic jet actuators and the control system was configured to minimize rms fluctuations at either one, or three control points. Two series of experiments were conducted - one to minimize the rms fluctuations in the buffer region of the turbulent boundary layer, and a second to minimize the wall-pressure fluctuations at an array of wall-pressure sensors.

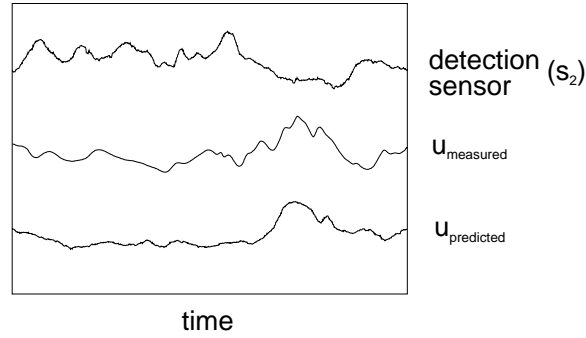


Figure 12: Time series showing the middle detection sensor signal, the measured and predicted stream-wise velocity ( $300l^*$  downstream of the actuator) and the input signal to the actuator. The signals were recorded with the actuator disconnected.

## 5.2 Forward Prediction

### 5.2.1 Conditioned Spectral Response

As described in section 4.2, the conditioned spectral response (CSA) was used to emphasize coherent structures common to two adjacent sensors. Figure 11, shows the structure of the CSA filter,  $L_{12}$ , that was derived from two adjacent spanwise wall-shear sensors, separated by  $40l^*$  in the spanwise direction. As one might expect, it has the form of a low-pass filter, emphasizing the low frequencies that are associated with the elongated low-speed streaks. It should be noted that a property of the FIR filter that results from the CSA procedure is that the resultant feature has linear phase, the slope of which represents the average advection time between the two sensors. In this case, since the two sensors are side-by-side with no streamwise offset, the phase is identically zero.

Signals from the three shear sensors,  $s_1$ ,  $s_2$  and  $s_3$  (each separated by  $40l^*$  in the spanwise direction) were pre-conditioned using the CSA technique, yielding  $s_{12}^c$ ,  $s_{21}^c$ ,  $s_{23}^c$  and  $s_{32}^c$ . Several combinations of raw input signals and conditioned signals were used to compute the forward predictor,  $\hat{H}$  and it was found that a weighting of the centerline raw signal, and the four CSA signals yielded the best forward predictor that could predict the velocity fluctuations  $300l^*$  downstream with an rms error of only 2.9%. A sample time-trace of the center line input signal,  $s_2$ , the predicted velocity fluctuation  $300l^*$  downstream and the measured velocity fluctuations is shown in figure 12. Comparing the measured and predicted velocity signals, it is clear that the large scale motion, high amplitude peaks and periods of activity and lull are successfully captured.

### 5.2.2 Optimal Linear Prediction: Wall Pressure Versus Streamwise Velocity Fluctuations

The characteristics of the predictive filters are illustrated in figure 13. The optimal transfer functions for the streamwise velocity is shown in figure 13a. The emphasis is on the low frequencies ranging up to the inertial scales. The filters for predicting the wall pressure signal are also shown in figure 13b and tend to emphasize higher frequencies indicating the pressure (the output) is a function of the derivative of the upstream shear sensor signals. The low-frequency slope is approximately equal to 1 which corresponds to a first derivative in the time domain ( $\partial/\partial t = i\omega$ , where  $i = \sqrt{-1}$ ). This observation in the difference between the predictive filters for velocity and pressure is consistent with previous conditionally sampled results by Johansson *et al.* (1991), who show that the high amplitude pressure peaks coincide with large positive gradients in the streamwise velocity fluctuations (indeed, the linearized Navier-Stokes equations show this relationship).

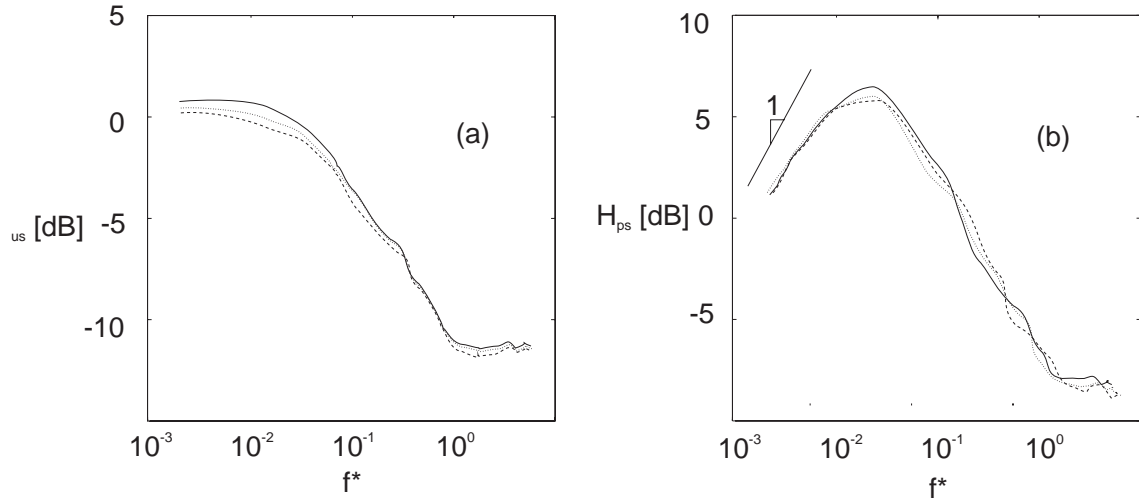


Figure 13: Optimal multiple-input/single-output transfer functions for the three detection sensors for the prediction of (a) streamwise velocity  $300l^*$  downstream at  $y^+ = 10$  and (b) wall pressure  $500l^*$  downstream.

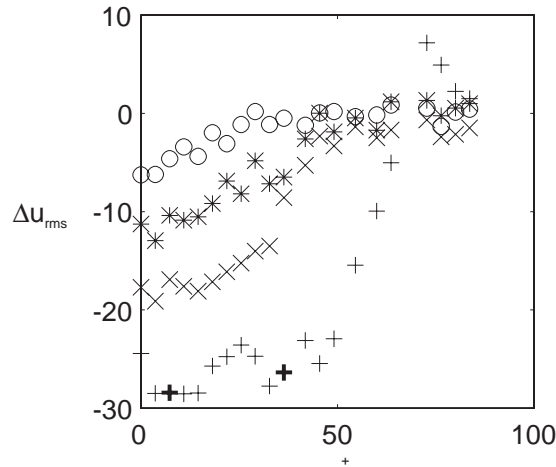


Figure 14: Percentage change of the streamwise velocity fluctuation with spanwise distance from the center actuator at four streamwise stations downstream of the actuator array;  $x^+ = 20, 100, 300$  and  $500$ . The bold pluses indicate the points of optimization ( $z^+ = 5, z^+ = 45$ ).

### 5.3 Multiple-Input/Multiple-Output control

The linear prediction discussed above was extended to predict the velocity fluctuation fields at three control points, as shown in figure 9. In addition, the three actuators were coupled in to the control system, as described earlier. The multiple-input/multiple-output prediction procedure was used together with the pre-conditioning of all three detection sensors to emphasize the large scale motion. The complete system was implemented in real-time with the control objective to minimize the rms-fluctuations in the streamwise velocity signal at three control points located at  $y^+ = 10$ . The control points were located  $20l^*$  downstream of the actuator array.

A summary of the control performance is shown in figure 14 which shows the percentage reduction in the streamwise rms-fluctuations as a function of the spanwise distance. Several  $x$ -locations are shown varying from  $20 x^*$  behind the actuators to  $500 x^*$  downstream of the actuator array. Focussing first on the “plus” symbols which shows that there is a broad and uniform strip of controlled flow in which the rms-fluctuations are reduced by approximately 28%. The two bold symbols represent the control points, at which the control system was optimized. However, note that the controlled area is

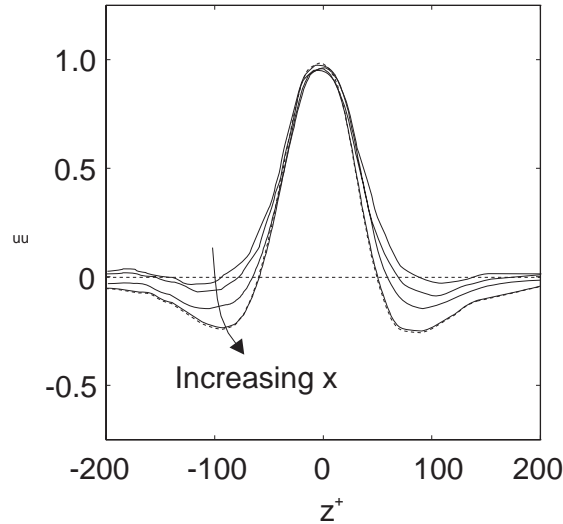


Figure 15: Spanwise spatial correlations downstream of the actuator array with increasing  $x$ .

reasonably uniform across the span in between the control points, and that it degrades quickly, but gracefully as  $z$  increased beyond the area of the actuators. There is also a slight overshoot, at  $z^* = 70$  where the rms fluctuations are actually greater than in the uncontrolled case. Although this is an isolated region, and probably not worth worrying about, Rathnasingham & Breuer (2002) describe how the overshoot can be eliminated with a small modification to the basic control algorithm.

The controlled flow degrades slowly as one moves downstream and by about 500 wall units downstream, the reduction in rms-fluctuations has decreased to about 7%. This suggests that the region of controlled flow is relaxing back to its uncontrolled state. It was shown (Rathnasingham & Breuer, 2002) that the cause of this is primarily due to entrainment from the sides of uncontrolled turbulence, rather than internal decay of the controlled state. This was demonstrated by comparing the relaxation of three-actuator control states with that of one-actuator control states.

The spanwise spatial velocity correlation at four streamwise stations downstream of the actuator array is shown in figure 15. The correlation corresponding to the unforced flow is shown by the dashed line. At the point of optimization ( $x^+ = 20$ ), the location of the minimum point and the point of zero crossing have been forced out further in the spanwise direction. This indicates that the coherent structures that now exist, as a result of the control, are more widely spaced in the spanwise direction. They are also much weaker as indicated by reduced negative correlation at the minimum point. The correlation curve recovers to the unforced curve as the streamwise station moves further downstream. The implication in this modification of the spatial correlation is that the introduction of the streamwise vortices into the flow to ‘cancel’ coherent structures achieves its desired control result (in this case, a reduction in the streamwise velocity fluctuations) by interacting with the flow in such a way so as to increase the spanwise separation of the large-scale, energy producing structures, while weakening their relative correlation with each other. In other words, the break-up of the coherent structures is achieved by weakening their ability to interact with each other.

#### 5.4 Effects on the Wall Shear Stress

Although the current experiment did not explicitly try to reduce the mean velocity shear stress, the effect of the current control algorithm on the mean shear was measured, and is shown in figure 16a, which shows the mean velocity profile, with and without active control. Clearly the slope decreases when control is applied, suggesting that the mean shear is decreased. An estimate of this, by fitting a line to the velocity profile suggests that the mean shear is reduced by about 7%. Although this is only a qualitative measurement of the wall shear, the measurement was taken with the hot-wire fixed at each location while the control was switched on and off. Thus it illustrates a definite and

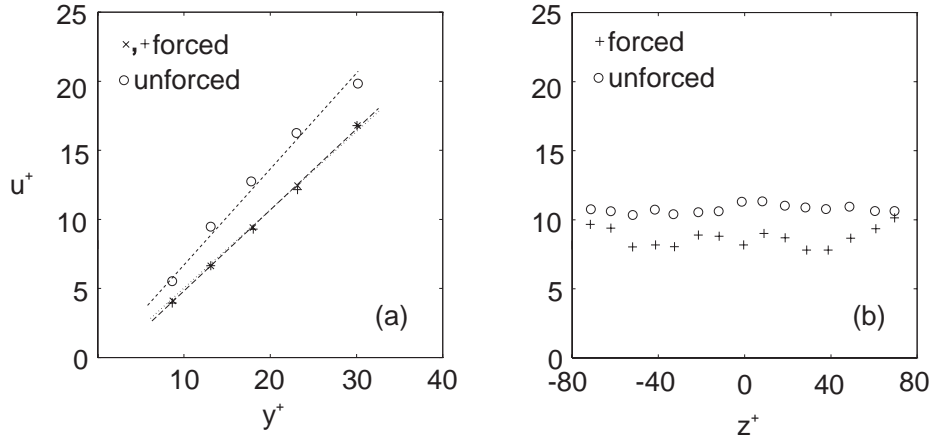


Figure 16: Mean velocity profile near the wall for the forced and unforced cases, (a) in the wall-normal direction at  $z^+ = 10$ , the shear is reduced by approximately 7% in the forced case; (b) in the spanwise direction, at  $y^+ \approx 15$ , the velocity is reduced throughout the control region.

marked reduction and shows promise for future work in drag reduction. Figure 16b is a plot of the mean velocity profile in the spanwise direction taken at  $y^+ = 15$ . It shows that the reduction in the mean velocity extends over the entire spanwise extent of the controlled region, suggesting that the reduction in shear is not localized close to the actuators. This result is extremely encouraging, since it suggests that had the primary control objective been to reduce the wall shear (instead of to reduce the rms-fluctuations), then perhaps even greater wall shear reductions would have been realized.

## 6 Conclusions

Over the course of approximately ten years, the design and fabrication of MEMS shear sensors has come a long way and much has been learned both in fabrication processes and in their application to aerodynamic measurements of shear. The tradeoffs between floating element (direct measurement) shear sensors and thermal element (indirect measurement) are complex, application-specific and there is no one approach that will solve all problems. However, what is important is that the advantages and limitations, as have been outlined here, are understood. We have demonstrated the design, fabrication and testing of new shear stress and temperature sensors which use a thermal sensing principle familiar to the "macro" world. Indeed, one lesson learned is that the scaling of MEMS thermal devices does not necessarily favor their implementation at the small scale. The high surface areas result in large parasitic losses, which need to be carefully controlled in order to achieve a sensor, which appreciable performance. The present devices have been found to be robust and to have good sensitivity for measurements in air. Measurements in other fluids, such as water, should be possible, although an insulating layer, might need to be deposited over the sensor element to prevent electrical shorts in a conducting medium. What makes the current devices somewhat distinct is that the supporting membrane in the present case is very thin (1500-Å). This substantially reduces the heat lost to the surrounding substrate. A second distinction is the use of platinum as the sensor element. Platinum has some advantages over polysilicon in that the platinum sensor resistance is typically much lower and the metal has a higher temperature coefficient of resistivity. All of these effects contribute to a sensor with improved sensitivity and lower noise characteristics.

The situation for actuators is far less well developed and although we have focussed on synthetic jets which have shown much promise, particularly in separation control experiments, it is by no means clear that this is the best approach for wall-based control, in the long run. The devices are difficult to design and incorporate into an experiment. They are very inefficient (due to the high viscous losses

of the fluid moving in and out of the actuator slit) and are prone to failure due to clogging and the high cycle fatigue that they experience during their operation. However, at the present there is little else available and more work needs to be done in this area.

Finally, the coordination of these devices - the feedforward control algorithm - represents the largest opportunity for progress. There is encouraging work on theoretical and numerical experiments on control which, while interesting, has so far been completely inapplicable to the real world. At the same time, the current approach, while relatively easy to implement and surprisingly successful, can surely be improved with more sophistication that CFD and DNS can provide - the two extremes can and will meet to close this gap.

## Acknowledgments

This paper contains a compilation of research, much of which has been published in journals and/or presented at conferences sponsored by AIAA, ASME and IEEE. The author gratefully acknowledges the support of AFOSR and DARPA over the years, as well as the immeasurable contributions from Ruben Rathnasingham, Keith Amonlirdviman, Marty Schmidt, Robert Bayt, Anju Nayyar, Howard Goldberg, Aravind Padmanabhan and Mark Sheplak.

## References

- ADRIAN, R. 1994 Stochastic estimation of conditional structure - A review. *Applied Scientific Research* **54** (3-4), 291 – 303.
- ALMONLIRDVIRMAN, K. A. & BREUER, K. S. 2000 Linear predictive filtering in a turbulent channel flow. *Phys. Fluids* **12** (12), 3221–3229.
- BENDAT, J. & PIERSOL, A. 1971 *Random Data: Analysis and Measurement Procedures*. New York, New York: Wiley-Intersciences.
- BEWLEY, T. 2001 Flow control: New challenges for a new renaissance. *Progress in Aerospace Sciences* **37**, 21–58.
- BEWLEY, T., MOIN, P. & TEMAM, R. 2001 DNS-based predictive control of turbulence: an optimal benchmark for feedback algorithms. *J. Fluid Mech.* **447**, 179–225.
- BREUER, K., BAYT, R. & NAYAAR, A. 1999 Mems-based shear and temperature sensors. In *Proceedings of the Fourth Microfluidics Symposium*. ASME.
- BREUER, K., DZENITIS, M., GUNNARSSON, J. & ULLMAR, M. 1996 Linear and nonlinear evolution of roughness-induced disturbances in a laminar boundary layer. *Phys. Fluids* **8** (6), 1415–1423.
- CHOI, H., MOIN, P. & KIM, J. 1994 Active turbulence control for drag reduction in wall-bounded flows. *J. Fluid Mech.* **Vol. 262**, 75–110.
- COE, D., ALLEN, M., TRAUTMAN, M. & GLEZER, A. 1994 Micromachined jets for manipulation of macro flows. *Solid-State Sensor and Actuator Workshop* pp. 243–247.
- COLLER, B. D., HOLMES, P. & LUMLEY, J. L. 1994 Control of bursting in boundary layer modes. *Applied Mech. Rev.* **47** (6, Part 2), 139–149.
- GLEZER, A. & AMITAY, M. 2002 Synthetic jets. *Ann. Rev. of Fluid Mech.* **34**, 503–529.
- GOLDBERG, HOWARD, D., PIEPSZ, O., BREUER, K. S. & SCHMIDT, M. A. 1995 A silicon microfabricated hot-wire anemometer utilizing backside contacts. In *Proceedings of the ASME Symposium on Applications of Micromachining to Fluid Mechanics*. Chicago, IL.

- GROSJEAN, C., LEE, G., HONG, W., Y.C., T. & HO, C. 1998 Micro ballon actuators for aerodynamic control. In *Proceedings of the 11th International Workshop on Micro Electro Mechanical Systems (MEMS '98)*, pp. 166–171. Heidelberg, Germany.
- HUNT, J. & CARRUTHERS, J. 1990 Rapid distortion theory and the problems of turbulence. *J. Fluid Mech.* **212**, 497–532.
- INGARD, U. 1953 On the theory and design of acoustic resonators. *J. Acoustical Soc. of America* **25** (6), 1037–1060.
- JACOBSON, S. A. & REYNOLDS, W. C. 1998 Active control of streamwise vortices and streaks in boundary layers. *J. Fluid Mech.* **360**, 179–211.
- JOHANSSON, A. V., ALFREDSSON, P. H. & KIM, J. 1991 Evolution and dynamics of shear layer structure in near wall turbulence. *J. Fluid Mech.* **224**, 579–599.
- JOHANSSON, A. V., HER, J. & HARITONIDIS, J. H. 1987 On the generation of high amplitude wall-pressure peaks in turbulent boundary layers and spots. *J. Fluid Mech.* **175**, 119–142.
- KRAVCHENKO, A. G., CHOI, H. & MOIN, P. 1993 On the relationship between near-wall streamwise vorticities to wall skin friction in turbulent boundary layers. *Phys. Fluids* **5** (12), 3307 – 9.
- LANDAHL, M. T. 1990 On sublayer streaks. *J. Fluid Mech.* **212**, 593 – 614.
- LEE, C. & GOLDSTEIN, D. 2001 DNS of microjets for turbulent boundary layer control. AIAA Paper 2001-1013.
- LEE, C., KIM, J., BABCOCK, D. & GOODMAN, R. 1997 Application of neural networks to turbulence control for drag reduction. *Phys. Fluids* **9** (6), 1740 –1747.
- LEE, K. H., CORTELEZZI, L., KIM, J. & JASON, S. 2001 Application of reduced-order controller to turbulent flows for drag reduction. *Phys. Fluids* **13** (5), 1321 –1330.
- LIEPMANN, H. W., BROWN, G. L. & NOSENCHUCK, D. M. 1982 Control of laminar-instability waves using a new technique. *J. Fluid Mech.* **118**, 187–200.
- LORKOWSKI, T., RATHNASINGHAM, R. & BREUER, K. S. 1997 Small-scale forcing of a turbulent boundary layer. AIAA Paper 97-1792.
- LUI, C., TAI, Y.-C., HUANG, J.-B. & HO, C.-M. 1995 Surface micromachined thermal shear stress sensor. In *Proceedings of the ASME Symposium on Applications of Micromachining to Fluid Mechanics*. Chicago, IL.
- PADMANABHAN, A., GOLDBERG, H., BREUER, K. & SCHMIDT, M. 1996 A wafer-bonded floating element shear stress microsensor with optical position sensing by photodiodes. *J. Microelectromechanical Systems* **5**, 307–315.
- PODVIN, B. & LUMLEY, J. 1998 Reconstructing the flow in the wall region from wall sensors. *Phys. Fluids* **10** (5), 1182 – 1190.
- PURTELL, L., KLEBANOFF, P. & BUCKLEY, F. 1981 Turbulent boundary layers at low Reynolds numbers. *Phys. Fluids* **24**, 802–811.
- RATHNASINGHAM, R. 1997 System identification and active control of a turbulent boundary layer. *PhD. Thesis, Department of Aeronautics and Astronautics, MIT* (Also MIT FDRL Report 97-6).
- RATHNASINGHAM, R. & BREUER, K. S. 1997a Coupled fluid-structural characteristics of actuators for flow control. *AIAA J.* **35**, 832–837.

- RATHNASINGHAM, R. & BREUER, K. S. 1997*b* System identification and control of turbulent flows. *Phys. Fluids* **9** (7), 1867–1869.
- RATHNASINGHAM, R. & BREUER, K. S. 2002 Feedforward control of turbulent boundary layers. *J. Fluid Mech.* Submitted for publication.
- SCHLICHTING, H. 1968 *Boundary Layer Theory*. New York, New York: McGraw-Hill, Inc.
- SCHMIDT, M., HOWE, R., SENTURIA, S. & HARITONIDIS, J. 1988 Design and calibration of a microfabricated floating-element shear-stress sensor. *IEEE Transactions on Electron Devices* **ED-35**, 750–757.
- SHEPLAK, M., PADMANABHAN, A., SCHMIDT, M. & BREUER, K. 1998 Dynamic calibration of a shear stress sensor using stokes layer excitation. *AIAA J.* (In Press. Also AIAA Paper 98-0585).